



**Time-Resolved Molecular Frame Dynamics of
Fixed-in-Space CS₂ Molecules**

Christer Z. Bisgaard, *et al.*
Science **323**, 1464 (2009);
DOI: 10.1126/science.1169183

***The following resources related to this article are available online at
www.sciencemag.org (this information is current as of March 12, 2009):***

Updated information and services, including high-resolution figures, can be found in the online version of this article at:

<http://www.sciencemag.org/cgi/content/full/323/5920/1464>

Supporting Online Material can be found at:

<http://www.sciencemag.org/cgi/content/full/323/5920/1464/DC1>

This article **cites 28 articles**, 8 of which can be accessed for free:

<http://www.sciencemag.org/cgi/content/full/323/5920/1464#otherarticles>

This article appears in the following **subject collections**:

Chemistry

<http://www.sciencemag.org/cgi/collection/chemistry>

Information about obtaining **reprints** of this article or about obtaining **permission to reproduce this article** in whole or in part can be found at:

<http://www.sciencemag.org/about/permissions.dtl>

2a-f, yielding the homologous series of supramolecular complexes $1_{m+6}2_m$. In such complexes, the complementarity of size leads to a structure type that overrides the strong driving force of PFC-HC segregation. This process is expected to require surmounting a considerable energy barrier, especially in the case of the very long DIPFA **2c**. Although the size-matching leads to one product, the PFC-HC segregation does not distinguish between various sizes of PFC and HC segments, as was proven by the observation of a variety of complexes produced from a size-mismatched PFC-HC mixture. Despite a lack of porosity of the starting materials **1a-f**, the DIPFAs **2a-f** are readily transported through the solid until a thermodynamically stable porous structure is achieved. A comparison with the x-ray structure of the pure salt **1b** (Fig. 1A) suggests that once the size-matching DIPFA forms halogen bonds with the I^- ions, the $I^- \cdots I(CF_2)_m I^-$ superanion acts as a template of the porous structure observed by promoting the positional and/or orientational rearrangement of the hydrocarbon dications (analogously to the sliding filament model, such as what occurs between thick and thin filaments in myofibrils). Our results show the relevance of a supramolecular-templated assembly of dynamically porous materials.

Gas-solid reactions often entail profound transformations of the chemical and physical nature of the solid materials and rarely are of practical use. In the present case, the full reversibility of the process, whereby DIPFAs can first be selectively complexed and then quantitatively evacuated, yields purified fluorinated telomers and a reusable ionic scaffold. Beyond the practical potential for separating mixtures of α,ω -DIPFAs, we envision the appli-

cation of this purification method to another vast class of compounds of industrial interest, the α,ω -diiodoperfluoropolyethers (DIPFPEs), which are useful intermediates for the synthesis of fluoro-containing resins, elastomers, and surfactants.

References and Notes

- N. O. Brace, *J. Fluor. Chem.* **108**, 147 (2001).
- B. Ameduri, B. Boutevin, *Well-Architected Fluoropolymers: Synthesis, Properties and Applications* (Elsevier, Amsterdam, 2004).
- K. Baum, T. G. Archibald, A. A. Malik, *J. Org. Chem.* **59**, 6804 (1994).
- A. L. Logothetis, in *Organofluorine Chemistry*, R. E. Banks, B. E. Smart, J. C. Tatlow, Eds. (Plenum, New York, 1994), pp. 373–396.
- H.-P. Cao, Q.-Y. Chen, *J. Fluor. Chem.* **128**, 1187 (2007).
- S. J. Dalgarno, P. K. Thallapally, L. J. Barbour, J. L. Atwood, *Chem. Soc. Rev.* **36**, 236 (2007).
- P. Metrangolo, G. Resnati, *Chem. Eur. J.* **7**, 2511 (2001).
- K. Rissanen, *CrystEngComm* **10**, 1107 (2008).
- P. Metrangolo, G. Resnati, *Science* **321**, 918 (2008).
- P. Metrangolo, H. Neukirch, T. Pilati, G. Resnati, *Acc. Chem. Res.* **38**, 386 (2005).
- P. Metrangolo, F. Meyer, T. Pilati, G. Resnati, G. Terraneo, *Angew. Chem. Int. Ed.* **47**, 6114 (2008).
- M. I. Nelen, A. V. Eliseev, *J. Chem. Soc. Perkin Trans. 2* **1359** (1997).
- H.-G. Löhre *et al.*, *J. Org. Chem.* **49**, 1621 (1984).
- P. Sun, Q. Jin, L. Wang, B. Li, D. Ding, *J. Porous Mater.* **10**, 145 (2003).
- E. Menozzi, J. Rebek, *Chem. Commun. (Camb.)* **44**, 5530 (2005).
- Materials and methods are available as supporting material on Science Online.
- R. Liantonio, P. Metrangolo, T. Pilati, G. Resnati, *Cryst. Growth Des.* **3**, 355 (2003).
- A. Bondi, *J. Phys. Chem.* **68**, 441 (1964).
- M. W. Hosseini, J. M. Lehn, *J. Am. Chem. Soc.* **104**, 3525 (1982).
- S. Boneva, St. Kotov, *Chromatographia* **25**, 735 (1988).
- H. Dindi, J. J. Hagedorn, M.-H. Hung, U.S. Patent 6825389 (2004).

- J. L. Atwood, L. J. Barbour, A. Jerga, B. L. Schottel, *Science* **298**, 1000 (2002).
- P. K. Thallapally *et al.*, *Nat. Mater.* **7**, 146 (2008).
- B. D. Chandler *et al.*, *Nat. Mater.* **7**, 229 (2008).
- J. L. Atwood, L. J. Barbour, A. Jerga, *Science* **296**, 2367 (2002).
- S. Kitagawa, K. Uemura, *Chem. Soc. Rev.* **34**, 109 (2005).
- D. Braga *et al.*, *Angew. Chem. Int. Ed.* **45**, 142 (2006).
- J. J. Vittal, *Coord. Chem. Rev.* **251**, 1781 (2007).
- S. Libri *et al.*, *Angew. Chem. Int. Ed.* **47**, 1693 (2008).
- P.M., T.P., and G.R. thank Fondazione Cariplo (Project "Self-Assembled Nanostructured Materials: A Strategy for the Control of Electrooptic Properties") for generous support. K.R. thanks the Academy of Finland (project 212588) for generous support. A.V. thanks the U.S. Air Force Research Laboratory/Air Force Office of Scientific Research for a generous Window on Europe grant, A. Garscadden for his endorsement, and R. Channell, R. Corley, and M. Huggins for their support. The authors declare no conflict of interest. A part of the present work is the object of the patent application PCT/EP2008/058588 (2008), priority date 7 November 2007, by Y.C., P.M., and G.R. to Politecnico di Milano. The authors' contributions were as follows: A.V., Y.C., M.L., T.P., and P.M. performed experiments; P.M., G.R., K.R., M.L., T.P., and Y.C. performed data analysis; and P.M., G.R., K.R., M.L., and T.P. wrote the paper. Crystallographic data for compounds **1a•2a**, **1a•2b**, **1b•2b**, **1b•2d**, **1b**, and **1c•2c** can be obtained free of charge from the Cambridge Crystallographic Data Centre via www.ccdc.cam.ac.uk/data_request/cif under reference numbers CCDC 709470 to 709475, respectively.

Supporting Online Material

www.sciencemag.org/cgi/content/full/323/5920/1461/DC1
Materials and Methods
Figs. S1 to S30
Tables S1 to S10
Schemes S1 to S2
References

18 November 2008; accepted 22 January 2009
10.1126/science.1168679

Time-Resolved Molecular Frame Dynamics of Fixed-in-Space CS_2 Molecules

Christer Z. Bisgaard,¹ Owen J. Clarkin,^{1,2} Guorong Wu,¹ Anthony M. D. Lee,^{1,2*} Oliver Geßner,³ Carl C. Hayden,⁴ Albert Stolow^{1,2,†}

Random orientation of molecules within a sample leads to blurred observations of chemical reactions studied from the laboratory perspective. Methods developed for the dynamic imaging of molecular structures and processes struggle with this, as measurements are optimally made in the molecular frame. We used laser alignment to transiently fix carbon disulfide molecules in space long enough to elucidate, in the molecular reference frame, details of ultrafast electronic-vibrational dynamics during a photochemical reaction. These three-dimensional photoelectron imaging results, combined with ongoing efforts in molecular alignment and orientation, presage a wide range of insights obtainable from time-resolved studies in the molecular frame.

Most molecules are non-spherical and so exhibit a dependence on their relative orientation in interactions with other molecules or with light. Measurements, therefore, should ideally be made in the molecular reference frame (MF). Unfortunately, in the gas and liquid phases, molecules are generally ran-

domly oriented in the laboratory frame (LF) to which most standard techniques are referenced, leading to blurred observations of molecular properties and processes. An analogy is the difference between single-crystal versus powder x-ray diffraction, the former revealing the greatest details of molecular structure. Other examples

include the determination of vector correlations in photodissociation dynamics (1) and measurements of (time-independent) photoelectron angular distributions (PADs) of fixed-in-space molecules, which has been a goal of researchers since the 1970s (2) and was achieved for selected cases (3, 4). Promising ultrafast techniques for imaging structural and electronic changes during molecular processes, such as time-resolved x-ray (5) and electron (6, 7) diffraction, tomographic orbital imaging (8), time-resolved photoelectron spectroscopy (TRPES) (9, 10), laser-induced electron diffraction (11), and high harmonic generation (12), would all benefit from avoidance of this

¹Steele Institute for Molecular Sciences, National Research Council Canada, 100 Sussex Drive, Ottawa, Ontario K1A 0R6, Canada. ²Department of Chemistry, Queen's University, Kingston, Ontario K7L 3N6, Canada. ³Chemical Sciences Division, Lawrence Berkeley National Laboratory, One Cyclotron Road, M/S 2-300, Berkeley, CA 94720, USA. ⁴Combustion Research Facility, Sandia National Laboratory, Livermore, CA 94551, USA.

*Present address: Department of Cancer Imaging, BC Cancer Research Centre, Vancouver, British Columbia V5Z 1L3, Canada.

†To whom correspondence should be addressed. E-mail: albert.stolow@nrc.ca

orientational averaging of MF observables. Here we present ultrafast time-resolved imaging measurements of a complex molecular process (a non-adiabatic photochemical reaction) from the MF, employing a laser technique that transiently fixes the molecules' alignment in space for sufficiently long to permit field-free dynamic measurements.

Strong nonresonant laser fields can induce molecular axes alignment within the LF (13) but may themselves modify excited-state dynamics (14). The goal of probing molecules that are aligned but field-free can be accomplished by applying a short laser pulse (15) that leaves the molecules transiently aligned (fixed-in-space) for, typically, a few picoseconds. This very brief molecular alignment can only be fully exploited by ultrafast measurement techniques—in our case, by TRPES, a method sensitive to both electronic and vibrational rearrangements (16–19). We chose to investigate the nonadiabatic photodissociation reaction $\text{CS}_2 + h\nu \rightarrow \text{CS}_2^* \rightarrow \text{CS}(\text{X}) + \text{S}(\text{D})/\text{S}(\text{P})$. CS_2 is notable as a triatomic system because it exhibits three general features of photodissociation dynamics: (i) vibrational mode coupling, (ii) internal conversion, and (iii) intersystem crossing. Consequently, CS_2 has complex photodissociation dynamics and, despite numerous studies, many details remain unresolved (20). Our study of coupled electronic and vibrational rearrangements occurring during this reaction combined impulsive alignment (15) with time-resolved photoelectron three-dimensional (3D) imaging (10) and quantum beat spectroscopy (21) to reveal details of the scattering resonances discernable only within the MF.

The ultraviolet (UV, 200 nm) photodynamics of the initially linear CS_2 molecule involves complex nonadiabatic and spin-orbit mixing, leading to multiple product states. The excitation from a nonbonding S atom orbital to an antibonding π^* molecular orbital lengthens the C–S bonds and leads to a bent equilibrium geometry. Thus, the absorption spectrum contains progressions assigned to combined excitations of the symmetric stretch and bend vibrations. In addition, non-adiabatic interactions with a nearby excited state lead to the mixing of electronic character at bent geometries. The excited-state bending frequency is nearly degenerate with that of the considerably weakened symmetric stretch, leading to combination bands of symmetric stretch and bend with peaks spaced by $\sim 400 \text{ cm}^{-1}$, each further split ($\sim 30 \text{ cm}^{-1}$) because of this near degeneracy (22). The barrier to linearity in this electronically excited state is at $\sim 49600 \text{ cm}^{-1}$ (201.6 nm), the excitation energy used in our experiments. Therefore, Franck-Condon (FC) factors favor excitation into a quasi-linear geometry. Because photoabsorption leads to dissociation, these spectral peaks may be understood as photodissociation scattering resonances having lifetimes exceeding several vibrational periods. The two open product channels, $\text{CS} + \text{S}(\text{P}_j)$ and $\text{CS} + \text{S}(\text{D}_2)$, have a wavelength-dependent branching ratio (23) and broad translational energy distributions (24). From the peak

widths in the absorption and S atom action spectra, with estimated resonance lifetimes of $< 1 \text{ ps}$ (23). Femtosecond time-resolved ion yield (25, 26) and photoelectron (20) measurements confirmed this subpicosecond behavior. Coexisting with the sharp resonances in the 6-eV region is a broad underlying continuum (23) attributable to very short-lived scattering resonances (direct dissociation) involving the antisymmetric stretch vibration (27).

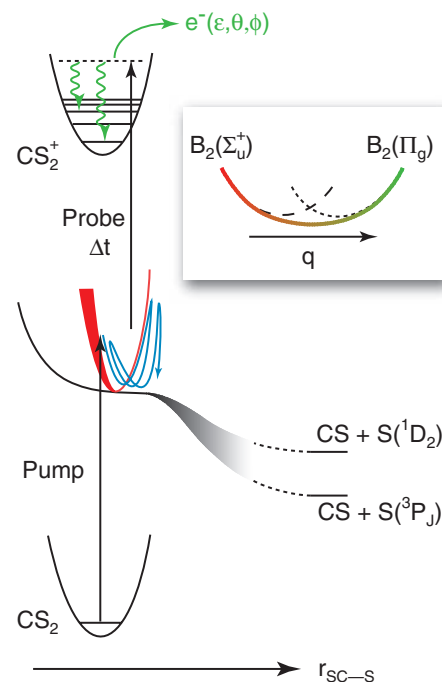
A depiction of our time-resolved photoelectron probing of CS_2 photodissociation dynamics is presented in Fig. 1. After transient alignment of the CS_2 , a femtosecond UV pump pulse prepared a coherent superposition of scattering resonances in a linear geometry, leading to quasi-bound vibrational motions followed by dissociation to both singlet and triplet products (Fig. 1). This superposition was probed as a function of time by a delayed probe pulse (125-fs pump-probe cross-correlation) that ionized the molecule. The emitted photoelectron was analyzed as a function of energy, 3D recoil angle, and pump-probe delay. The duration of the alignment ($\sim 4 \text{ ps}$ full width at half maximum) was longer than the time scale of the photoreaction ($< 1 \text{ ps}$), rendering the molecules effectively fixed in space during the measurement.

The resolved series of resonances allowed us to combine our time-resolved photoelectron 3D imaging method (28) with another powerful technique for probing excited-state dynamics: quantum beat spectroscopy (21). By tuning the central wavelength (bandwidth $\sim 250 \text{ cm}^{-1}$) of our femtosecond pump laser to 201.2 nm, we coherently prepared a superposition of two scattering resonances, differing only in the degree of symmetric stretch versus bending excitation. Quantum interference in photoionization of coherently prepared scattering resonances was previously reported in ion yield measurements for IBr (29) and CS_2 (26)

photodissociation. In the present case, the quantum beat interference between two long-lived scattering resonances in our MF photoelectron data permits access to intimate details of the electronic-vibrational couplings associated with the decay of these resonances.

A time-resolved photoelectron spectrum acquired for unaligned CS_2 is given in Fig. 2A, showing photoelectron kinetic energies as a function of delay. At short delays, the 0.7-eV peak, broadened because of an unresolved 55-meV spin-orbit splitting, arises from ionization into the vibrationless (0,0,0) cation ground state. The low-energy features correspond to ionization into highly excited vibrational states. The time-resolved spectrum is composed of a fast initial decay, as well as a slow decay across the whole spectrum, and a slow, periodic modulation of the high-energy electrons. We employed 2D global methods to simultaneously fit all photoelectron energies at all time delays to within experimental errors. Our kinetic model involved two independent exponential decays, with the longer one modulated by a harmonic oscillation (28). The global fit yielded time constants of $\tau_1 = 70 \pm 20 \text{ fs}$ and $\tau_2 = 830 \pm 40 \text{ fs}$, with a modulation period of $T = 1010 \pm 20 \text{ fs}$. The decay-associated photoelectron spectra of these three kinetic components are presented in Fig. 2B. As expected, the long-lived τ_2 component samples highly distorted geometries that ionize to vibrationally excited ions (low photoelectron energies). In Fig. 2C, we show the time evolution of the LF photoelectron signal at 0.7 eV and the global fit (red line), corresponding to ionization into the cation (0,0,0) ground state. The quantum beat signal can be clearly seen. The extracted time constant τ_2 is in very good agreement with the lifetime estimated from analysis of rotational band contours in the action spectrum (23). The

Fig. 1. Schematic representation of our femtosecond time-resolved photoelectron 3D imaging measurements of the predissociation dynamics of CS_2 . Dissociation proceeds via asymmetric stretching to singlet and triplet products. Because of the geometry change in the excited state, the initial nuclear motion proceeds along the bending and symmetric stretch coordinates (blue trajectory). Upon bending and stretching, the excited Σ_u^+ state adiabatically develops Π_g electronic character (inset). The quasi-bound dynamics are probed by measuring the energy and 3D emission direction of the photoelectrons emitted upon ionization into the bound ground state of the cation. q , a generalized vibrational coordinate; Δt , the pump-probe time delay; ε , kinetic energy; θ , the polar angle; ϕ , the azimuthal angle of the emitted electron.



1010-fs period matches the 34-cm^{-1} splitting observed at 201 nm in the absorption spectrum. We can, therefore, assign the periodic modulation to the quantum beat interference between the two quasi-bound scattering resonances. Our measurements confirm both the previously reported quantum beat (26) and the bi-exponential decay (20) measurements. The time constant τ_1 confirms the presence of broad, short-lived resonances (23). The laser alignment of CS_2 leaves these global time constants unchanged (i.e., the fitted MF and LF time constants are the same), suggesting that ground-state vibrations are not excited by the alignment laser.

This kinetic model of CS_2 excited-state decay reveals insufficient details of the underlying electronic-vibrational dynamics of the resonance decay. To advance, we applied the transient alignment method to make MF measurements. In Fig. 3, we show the two-photon ion yield as a function of the delay between the alignment pulse and the 201-nm pump pulse, in the vicinity of the rotational half-revival (greatest alignment). To quantify the alignment, we carried out simulations taking into account thermal averaging, spatial focal volume averaging over laser intensities, and the relative magnitudes of the parallel versus perpendicular ionization transition dipoles (28). The red curve in Fig. 3 shows the best fit to a degree of alignment of $\langle \cos^2\theta \rangle = 0.55 \pm 0.07$. Within the pump-probe window (<1.5 ps) across which MF time-resolved measurements were carried out, the molecules were effectively fixed-in-space.

To acquire time-resolved MF PADs of CS_2 photodissociation, we set the delay between the alignment and pump pulses to 73.5 ps, slightly before the maximal alignment. The 201-nm fs pump pulse, polarized parallel to the alignment axis, interacted with this aligned sample. Because of the parallel transition dipole, excitation further sharpened the excited-state alignment to an estimated value of $\langle \cos^2\theta \rangle = 0.74$. Energy-resolved PADs resulting from photoionization due to the

268-nm fs probe laser, also polarized parallel to the alignment axis, were recorded as a function of pump-probe delay within the time window shown in Fig. 3. The MF PADs for ionization into the (0,0,0) state of the cation (Fig. 2C) are shown at five time delays on the right side of Fig. 4. The analogous PADs for the unaligned sample are given on the left. A dramatic change in the MF PADs is observed in the photoelectron intensity parallel to the MF axis. At early times there is a local minimum along the MF direction, whereas at $t = 500$ fs there is a maximum in this direction. At $t = 900$ fs, the MF PAD has mostly reverted back to its form at $t = 100$ fs. As confirmed by the time scale, this occurs because of the quantum beat interference in the MF PAD between the two scattering resonances.

The selection of the MF PADs in Fig. 4 from the (0,0,0) cation ground state has important implications for the analysis of their structure and time evolution. First, FC factors restrict photoionization to quasi-linear geometries, simplifying a symmetry analysis. Second, photoionization of either scattering resonance produced the same cation vibrational state. Within the Born-Oppenheimer and FC approximations, electronic and nuclear dynamics are fully separated, and both resonances should produce the same PADs (i.e., the free electron departs from the same ion core), differing only in amplitude because of their distinct FC factors. If the PAD shape also varies during the quantum beat, as in Fig. 4, then the PADs from the two scattering resonances must differ in form. This means that there must be a vibrational coordinate dependence to the ionization transition dipole, a failure of the FC approximation.

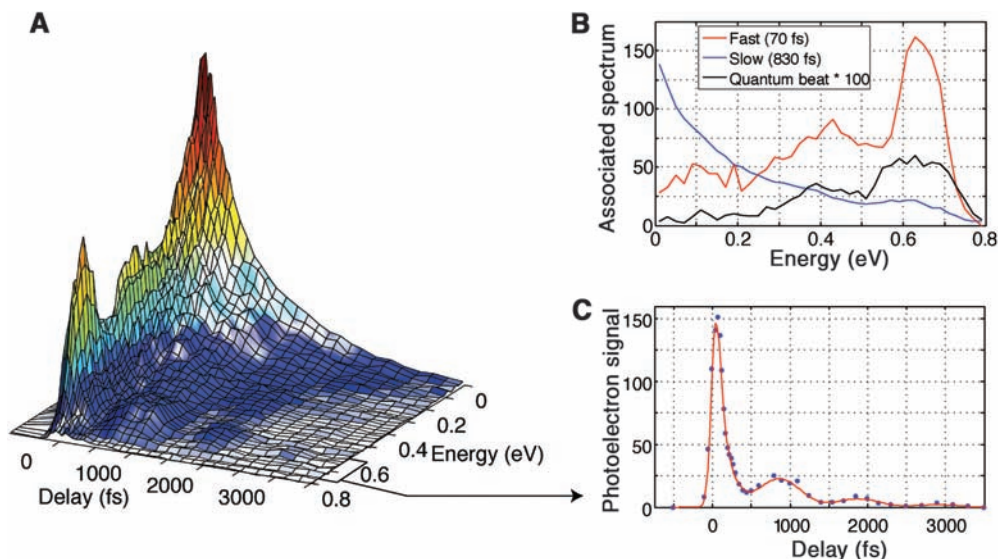
This coordinate dependence can originate from the variation of electronic structure with vibrational coordinates in the final continuum state, the neutral excited state, or both. Our final state is the (0,0,0) state of the strongly bound cation: The vibrational wave function is restricted to a small range of internuclear distances where we do not expect mixing with other cation electronic states.

We also argue that there are no resonances in the ionization continuum within our range of energies [see the supporting online material (SOM) text]. Therefore, neither the cation nor the free-electron wave function probably has strong vibrational coordinate dependence. It is rather the nuclear coordinate dependence of the electronic character of the excited neutral state that causes the PADs to evolve during the quantum beat and signifies the differential electronic character sampled by the different vibrational excursions of the two scattering resonances.

The above explanation is strongly supported by theory. In our case, one scattering resonance has more symmetric stretch character and less bend amplitude, whereas the other has the opposite. Energetically located just above the linear initial state ($^1\Sigma_u^+$) is an optically dark state ($^1\Pi_g$). In linear geometries, these two states do not interact. Upon bending, however, the degenerate upper state splits into two components, one of which interacts strongly with the initial state when bending and stretching. Therefore, as shown in the inset of Fig. 1, we expect mixing of Π_g character into the wave function as the molecule bends and stretches (q in Fig. 1). We thus attribute the time evolution of the MF PADs in Fig. 4 to the difference in bending and stretching amplitude between the two scattering resonances, sampling different degrees of Π_g character upon vibration. Our calculations reveal a strong mixing between these states at very small bending angles (fig. S2 and SOM text).

A complete determination of the photoionization dynamics requires knowledge of the amplitudes and phases for all partial waves. Although approximate methods for determining photoionization amplitudes exist, calculating the phase shifts of all partial waves for excited states of a polyatomic molecule undergoing nonadiabatic dynamics is currently computationally intractable. Furthermore, attempts to extract amplitudes and phases directly from the data will not yield a unique fit to the PADs. Therefore, precluding a

Fig. 2. (A) Time-resolved photoelectron spectrum of CS_2 after excitation to the $^1\Sigma_u^+$ state pumped at 201.2 nm. The decay-associated spectra resulting from a 2D global analysis of the data are shown in **(B)**, with the photoelectron signal fit at all energies and all delays simultaneously. In **(C)**, we show the evolution of the photoelectron band corresponding to ionization into the vibrational ground state of the cation, along with the result of the global fit. The quantum beat can be clearly seen.



detailed analysis of the photoionization dynamics, we consider a symmetry analysis based on the quasi-linear behavior sampled by our (0,0,0) final state (28). The quantum beat phenomenon leads to signals that oscillate between the sum and the difference of the two ionization transitions. There-

fore, the PADs at $t = 100$ fs and 900 fs reflect the average electronic character of the two scattering resonances, whereas the PAD at $t = 500$ fs reflects the difference in electronic characters between the two. The symmetry-expected MF PAD from the initial state ($t = 100$ fs) has minima in directions

Fig. 3. Jet-cooled CS_2 molecules are transiently aligned by a short (100-fs), non-resonant (805-nm) laser pulse, creating a rotational wave packet. The alignment dynamics around the half-revival are monitored via the two-photon ionization yield (blue dots). To estimate the degree of alignment, we simulated the ion yield as a function of delay using direct integration of the time-dependent Schrödinger equation to propagate the rotational wave packet. The calculated axis angular distribution is shown in the inset for the ground-state (blue) and excited-state (red) molecules. Within the window used for the pump-probe experiment (red band), the molecules are fixed in space.

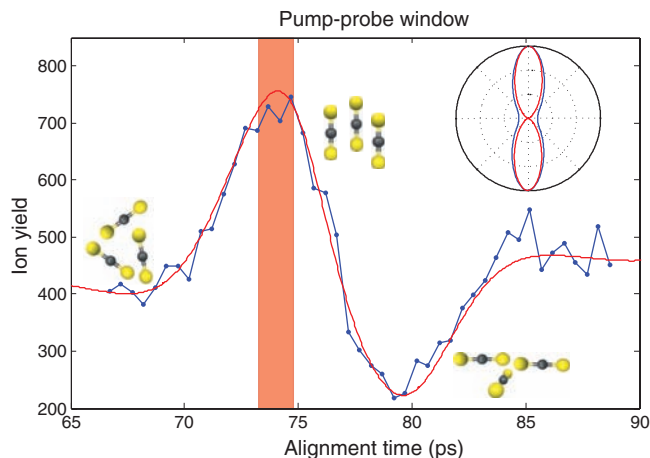
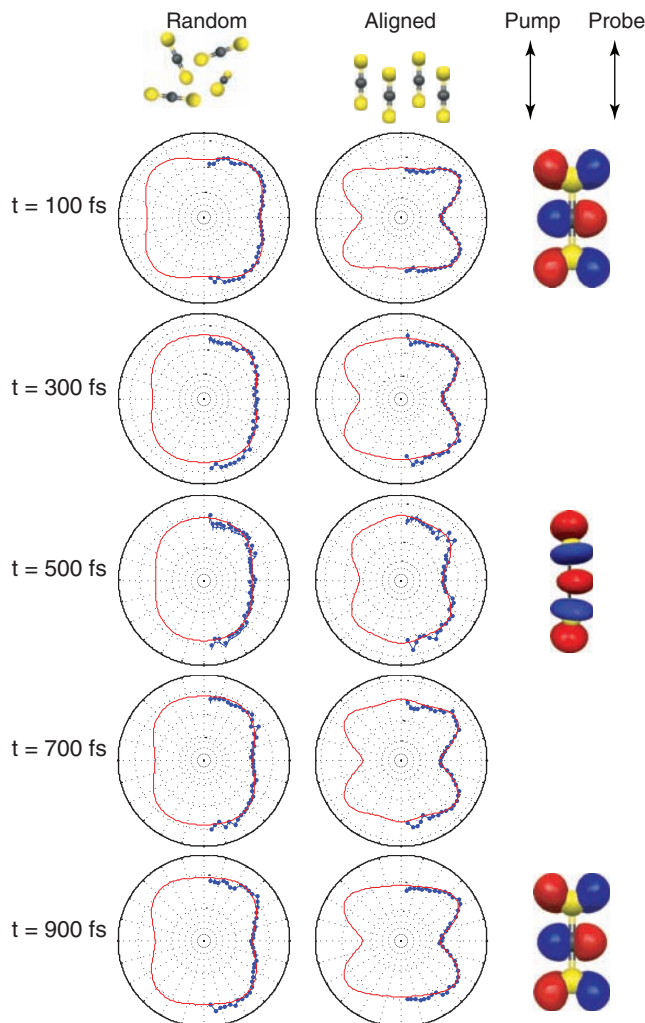


Fig. 4. Time-resolved PADs for unaligned (left) and aligned (right) CS_2 molecules. The LF laser polarization vectors are shown at top right. Also shown are the orbitals with the highest contribution to the state evolving adiabatically from the 1B_2 (Σ_u^+) state in the FC region. Top and bottom right panels show the π^* orbital that dominates in the FC region, whereas the middle right panel shows the σ^* orbital that contributes at geometries that are both stretched and bent. The MF PADs (aligned) reveal details of the dynamics not seen in the randomly aligned sample.



both parallel and perpendicular to the molecular axis. As seen from Fig. 4, this expectation is in good qualitative agreement (consistent with imperfect axis alignment) with the MF PAD observed at $t = 100$ fs. By $t = 500$ fs (corresponding to the minimum of the quantum beat in Fig. 2C), the angular distribution appears qualitatively different, now peaking parallel to the MF axis. The PAD observed at $t = 500$ fs is consistent with ionization from a state of Π_g symmetry, the expected difference between the two resonance wave functions. By $t = 900$ fs, approaching the first maximum of the quantum beat, the MF PADs again appears very similar to that at $t = 100$ fs.

Simplifying still further, if we employ single-active electron pictures, the MF PADs are directly determined by the initial orbital and the MF direction of the ionization transition dipole (19, 28). The changes in the PADs then directly reflect changes in orbital character. In the FC region, the initial state is predominantly of $n \rightarrow \pi^*$ character (the corresponding orbital is plotted at the top right of Fig. 4). As the molecule bends and stretches, state mixing introduces some $n \rightarrow \sigma^*$ character (middle right of Fig. 4). The qualitative changes in the MF PADs agree well with the changes in orbital character of the excited state, as the quantum beat phenomenon amplifies the differences between the two resonances. The MF PADs do show an energy dependence (fig. S1): Different ion vibrational states exhibit different PADs. However, their temporal evolution is very similar to that of the (0,0,0) state, with comparable changes at all energies. That the PADs are final state-dependent is consistent with the different ion states having different Condon points and, therefore, reflecting different aspects of the excited-state evolution.

The fact that the MF PADs exhibit an oscillatory behavior that is in phase at all energies highlights an important aspect of this observable (16). The time evolution of the PADs (Fig. 4) for fixed-in-space molecules is predominantly determined by changes in the electronic symmetry of the excited state. In contrast, the time evolution of the photoelectron spectrum (Fig. 2) is primarily sensitive to the vibrational dynamics and population decay: When several vibrational states of the cation are accessible, details of the dynamics may become obscured by averaging over these states. This is why the quantum beat is not observed in the photoelectron yield at low electron energies but stands out clearly in the MF PADs. In a simple model, the PADs are determined by the shape of the orbital being ionized and the ionic potential from which the electron is ejected. For small amplitude vibrational motion, which is ensured by our choice of final state, the changes in the PADs are then mostly determined by the re-organization of the electrons due to the coupling between electronic states. The time evolution of the photoelectron spectrum and the MF PADs, therefore, add complementary information about the dynamics, highlighting

the power of combining field-free alignment techniques with ultrafast spectroscopy.

References and Notes

1. T. P. Rakitzis, A. J. van den Brom, M. H. M. Janssen, *Science* **303**, 1852 (2004).
2. D. Dill, *J. Chem. Phys.* **65**, 1130 (1976).
3. J. H. D. Eland, *J. Chem. Phys.* **70**, 2926 (1979).
4. K. G. Low, P. D. Hampton, I. Powis, *Chem. Phys.* **100**, 401 (1985).
5. A. M. Lindenberg *et al.*, *Science* **308**, 392 (2005).
6. H. Ihee *et al.*, *Science* **291**, 458 (2001).
7. B. J. Siwick, J. R. Dwyer, R. E. Jordan, R. J. D. Miller, *Science* **302**, 1382 (2003).
8. J. Itatani *et al.*, *Nature* **432**, 867 (2004).
9. V. Blanchet, M. Z. Zgierski, T. Seideman, A. Stolow, *Nature* **401**, 52 (1999).
10. O. Geßner *et al.*, *Science* **311**, 219 (2006); published online 14 December 2005 (10.1126/science.1120779).
11. M. Meckel *et al.*, *Science* **320**, 1478 (2008).
12. W. Li *et al.*, *Science* **322**, 1207 (2008); published online 29 October 2008 (10.1126/science.1163077).
13. H. Stapelfeldt, T. Seidemann, *Rev. Mod. Phys.* **75**, 543 (2003).
14. B. J. Sussman, D. Townsend, M. Y. Ivanov, A. Stolow, *Science* **314**, 278 (2006).
15. F. Rosca-Pruna, M. J. J. Vrakking, *Phys. Rev. Lett.* **87**, 153902 (2001).
16. T. Seideman, *Annu. Rev. Phys. Chem.* **53**, 41 (2002).
17. K. L. Reid, *Annu. Rev. Phys. Chem.* **54**, 397 (2003).
18. T. Suzuki, *Annu. Rev. Phys. Chem.* **57**, 555 (2006).
19. A. Stolow, J. G. Underwood, *Adv. Chem. Phys.* **139**, 497 (2008).
20. D. Townsend *et al.*, *J. Chem. Phys.* **125**, 234302 (2006).
21. E. Hack, J. R. Huber, *Int. Rev. Phys. Chem.* **10**, 287 (1991).
22. R. J. Hemley, D. G. Leopold, J. L. Roebber, V. Vaida, *J. Chem. Phys.* **79**, 5219 (1983).
23. A. Mank, C. Starrs, M. N. Jago, J. W. Hepburn, *J. Chem. Phys.* **104**, 3609 (1996).
24. D. Xu, J. Huang, W. M. Jackson, *J. Chem. Phys.* **120**, 3051 (2004).
25. A. P. Baronavski, J. C. Owrutsky, *Chem. Phys. Lett.* **221**, 419 (1994).
26. P. Farmanara, V. Stert, W. Radloff, *J. Chem. Phys.* **111**, 5338 (1999).
27. R. R. Sadeghi, S. R. Gwaltney, J. L. Krause, R. T. Skodje, P. M. Weber, *J. Chem. Phys.* **107**, 6570 (1997).
28. Materials and methods are available as supporting material on *Science* Online.
29. M. J. J. Vrakking, D. M. Villeneuve, A. Stolow, *J. Chem. Phys.* **105**, 5647 (1996).
30. This work was supported by the Natural Sciences and Engineering Research Council of Canada (A.M.D.L. and A.S.). We gratefully acknowledge J. G. Underwood, S. Patchkovskii, C.-Y. Ng, M. Brouard, and D. M. Wardlaw for stimulating discussions.

Supporting Online Material

www.sciencemag.org/cgi/content/full/323/5920/1464/DC1
Materials and Methods
Figs. S1 and S2
References

1 December 2008; accepted 29 January 2009
10.1126/science.1169183

Clear Sky Visibility Has Decreased over Land Globally from 1973 to 2007

Kaicun Wang,^{1*} Robert E. Dickinson,² Shunlin Liang¹

Visibility in the clear sky is reduced by the presence of aerosols, whose types and concentrations have a large impact on the amount of solar radiation that reaches Earth's surface. Here we establish a global climatology of inverse visibilities over land from 1973 to 2007 and interpret it in terms of changes in aerosol optical depth and the consequent impacts on incident solar radiation. The aerosol contribution to "global dimming," first reported in terms of strong decreases in measured incident solar radiation up to the mid-1980s, has monotonically increased over the period analyzed. Since that time, visibility has increased over Europe, consistent with reported European "brightening," but has decreased substantially over south and east Asia, South America, Australia, and Africa, resulting in net global dimming over land.

Uncertainty about how much the concentration of atmospheric aerosols has increased over the past century and its impact on the global radiation balance have been major obstacles to establishing how observed changes of climate are related to changes in greenhouse gas concentrations. Some long-period observational constraints on aerosols are provided by measurement of solar radiation incident at the surface (1) and by estimation of emissions by fossil fuel combustion (2). The former can be equally or more greatly affected by changes of cloudiness (3), and the latter can be used to estimate changes of limited aerosol types (2). Much better estimates of global aerosol impacts can be made over the past decade from both surface and satellite measurements of aerosol optical depth (AOD) (4, 5). For a given vertical profile of aerosols, the meteorological visibility inverse (ViI) is directly proportional to AOD. Thus, we can use these recent measure-

ments of AOD to evaluate the accuracy of ViI in terms of its mean and spatial variability. This evaluation establishes the ViI climatology as a data set that characterizes the spatial and temporal variability of over-land aerosols for the past several decades.

We calculated ViI in km⁻¹ from the National Climatic Data Center (NCDC) Global Summary of Day (GSOD) database collected from about 3250 meteorological stations from 1973 to 2007. It is multiplied by a scaling factor of 1.0 km, as inferred from rules described in (6). This index is used as an estimate of AOD for a particular aerosol profile, and has other uncertainties described in (6). However, its evaluation against other more recent and more direct data sets shows that it estimates AOD with an accuracy comparable to that of the other measures (6) and thus can be used to discuss the effects of aerosols on the incidence of solar radiation.

The geographic long-term variation of this AOD measure is determined by aggregating the meteorological station data into continental regions where such data are available, removing time means, and calculating the area-weighted monthly anomaly values for regions where data are available for more than 80% of the stations [see

(6) for explanation of the gap; see fig. S7 for domains). Aerosols increased on average over all continental regions between 1979 and 2006, with the exception of Europe (Fig. 1). In particular, they increased from 1979 over Australia and south Asia (including India and China), decreased over South America and Africa from 1979 to about 1985, and then increased and were relatively unchanged over north Asia (Siberia).

The large increases of Asian AODs likely were consequences of large increases in industrial activities and are consistent with long-term observations of incident solar radiation and cloud cover in India (7) and China (8). The European decreases are consistent with numerous past studies based on long-term measurements of aerosols, solar radiation, and clouds (9–11), which are consistent with changes in emissions of aerosol precursors, SO₂ (12, 13), black carbon (14), and organic carbon (14, 15).

The variability of measured changes between stations from 1973 to 2007 is summarized in terms of linear trends for the period 1973 to 2007. Figure 2 shows the spatial distribution of the 58% of the stations that have magnitudes of their trends greater than 0.0015 year⁻¹—that is, 50% larger than the global area-weight average linear trend of 0.001 year⁻¹. This change in AOD is not the same everywhere; AODs substantially declined in Europe after peaking in the 1980s. These changes vary widely from location to location (Fig. 2). Overall, the largest increases of AOD have been in Asia, and these increases have accelerated over the past decade, producing the rapid global increase over this period.

Aerosols reduce solar radiation at Earth's surface by upward reflection and absorption. The energy lost in this manner either escapes to space or heats the air. Aerosols can further affect surface radiation by modifying cloud cover and other cloud properties. The long-term trend in over-land ViI AOD that we report is consistent with the long-term variation in incident solar radiation in China, India, and Europe (7–11). Wild *et al.* (1) documented that solar radiation

¹Department of Geography, University of Maryland, College Park, MD 20742, USA. ²Department of Geological Sciences, University of Texas, Austin, TX 78712, USA.

*To whom correspondence should be addressed. E-mail: kcwang@umd.edu